2026 IEEE International Conference on Robotics and Automation (ICRA 2026)
June 1-5, 2026. Vienna, Austria

Magnetic-Acoustic Microbubble Microrobot for Targeted Mechanical Stimulation of Cancer Cells

Cun Wang[1], Ruicheng Li[1], Qianyi Dai[1], Zhaokai Wang[1], Yongjun Lai[1], Lidan You[1], Xian Wang[1,2]

***Abstract*— Mechanical stimulation has recently been shown as a promising approach to induce targeted cancer cell death. With precise field control, magnetic microrobots were navigated to the tumor site for delivering mechanical stimulation as a new treatment approach. However, most magnetic microrobots suffer from low force output when generating mechanical stimulation. Acoustic microrobots, with a microbubble as their simplest form, generate strong mechanical stimulation yet lack precise position control. In this paper, leveraging the force output of the acoustic field and precision of magnetic field control, we present a magnetic acoustic microbubble microrobot (MAM) that integrates magnetic navigation and acoustic stimulation. MAMs were fabricated with DSPC/PEG lipid shells and iron-oxide nanoparticles (IONPs) using a flow-focusing microfluidic method. The size of the fabricated monodispersed MAMs is approximately 10 μm. The fabricated MAMs were navigated by a quadrupole magnetic tweezer system, with a maximum field gradient of 2–3 T/m, and controlled to oscillate to generate mechanical stimulation under an acoustic transducer at 1 MHz. As a proof-of-concept, we applied MAM acoustic treatment to breast cancers (MDA-MB-231) and showed that MAM acoustic treatment led to reduced cell viability compared to the control group and the acoustic-only group. Considering all the components for MAM fabrication are FDA-approved materials, MAM holds promise for clinical translation in tumor mechanical stimulations.**

I. INTRODUCTION

With recent advancements in mechanobiology for understanding how cancer cells sense force, mechanical stimulation has emerged as a powerful method for causing cell death [1], [2], [3]. Among the cancer cell stimulation methods, magnetic microrobots stand out with its deep tissue penetration and high precision [4], [5]. However, as the field gradient-based magnetic force decays quickly in space, delivering strong mechanical stimulation becomes a fundamental challenge.

Relying on a period acoustic field, acoustic methods, especially commonly-used microbubbles, can generate strong oscillations for mechanical stimulation, yet suffer from limited spatial control and targeting accuracy [6], [7]. Combining actuation from both the controllable magnetic and high-output acoustic fields could deliver precise and strong mechanical stimulation to individual cells in biological environments. Microbubbles are proven to be capable of force generation in the order of nanonewtons, sufficient to disrupt cellular membranes and cause cell death [8], [9]. Their biocompatibility and wide clinical use as contrast agents further support their potential in biomedical microrobotics. Functionalization of microbubbles with iron oxide nanoparticles would allow magnetic position control and acoustic-generated stimulation to apply targeted mechanical stimulation [10], [11] (Fig. 1).

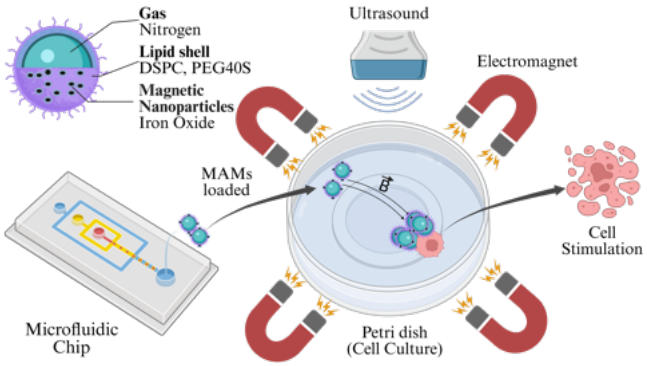

Fig. 1: Conceptual illustration of the proposed MAM cell disruption. MAMs fabricated from the microfluidic chip are magnetically guided to the target cell and then acoustically oscillated (via ultrasound) to disrupt cancer cells.

Key challenges remain in the deployment of MAMs as a robotic mechanical stimulation platform technology. First, the fabrication and collection of microbubbles with a consistent size is challenging due to their short half-time [12], [13]. Second, incorporating sufficient magnetic components without compromising acoustic response is difficult due to trade-offs in shell stiffness and microbubble stability [14]. Finally, a lack of a quantitative model for navigation and mechanical stimulation at the single bubble level hinders the precise control and reproducibility of stimulation [6].

In this work, we present an integrated magnetic-acoustic system designed to control magnetic-acoustic microbubbles (MAM) for targeted cell disruption. The MAMs were fabricated using a custom-made flow-focusing microfluidic chip. The control platform combines a robotic quadrupole magnetic tweezer system with a 1 MHz acoustic transducer to achieve control of 10 μm magnetic microbubbles within a 6 mm workspace. Further, we developed and validated the magnetic and acoustic model for the mechanical stimulation using MAMs. This system enabled targeted positioning of MAMs followed by ultrasonic oscillation to apply mechanical stress directly to cancer cells. Using breast cancer cells, we demonstrated that cell viability significantly decreased 24 hours after applying MAM acoustic treatment, providing direct evidence of mechanical disruption induced by the

*Corresponding author: xian.wang@queensu.ca
[1] Department of Mechanical and Materials Engineering, Queen's University, Kingston, Canada.
[2] Ingenuity Labs Research Institute, Queen's University, Kingston, Canada.

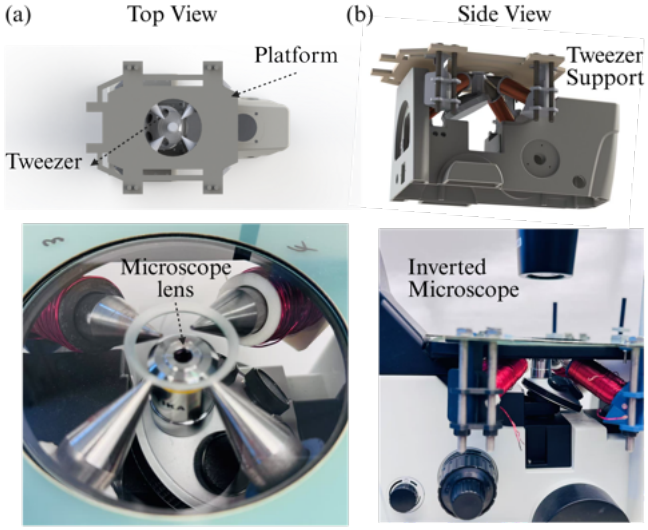

Fig. 2: Quadrupole magnetic tweezer system. a) The CAD design of the quadrupole magnetic tweezer assembly showing annotated components (top view). b) Side view rendering of the complete setup.

combined magnetic-acoustic actuation.

II. Systems and Experiments

A. Magnetic Actuation System

A compact quadrupole magnetic tweezer was built, adapted from [15], to actuate MAMs within a 6-mm microscope workspace (Fig. 2). Four identical electromagnets were symmetrically arrayed around the sample chamber and canted by 30° relative to the horizontal, generating simultaneous in-plane and out-of-plane field components for 3D force control. Each pole used a 20-mm-diameter iron core ($\sim$ 90% purity) machined to a 2-mm conical tip to concentrate magnetic flux in the workspace, and was wound with 300 turns of 20-AWG enameled copper wire. The magnet assemblies were mounted on 3D-printed supports fixed to a laser-cut acrylic frame, yielding a rigid, low-profile structure compatible with an inverted microscope stage (Fig. 2b). Coils are driven independently by OPA549 linear power amplifiers (±3 A per coil) commanded by two ESP32 microcontrollers and powered from two DC supplies. Field magnitude and gradients will be simulated via finite element analysis and calibrated by Hall-probe Gauss meter measurements. The tweezer is integrated with an inverted optical microscope (OPTIKA IM-300D) for real-time visualization, enabling coordinated magnetic positioning of MAMs before acoustic stimulation.

B. Acoustic Stimulation System

To achieve the mechanical stimulation of cancer cells within the target workspace via oscillating MAMs, we designed a compact acoustic stimulation system (Fig. 3). A 2-mm-thick piezo-ceramic ring transducer (inner diameter 10 mm, outer diameter 20 mm) is employed to generate

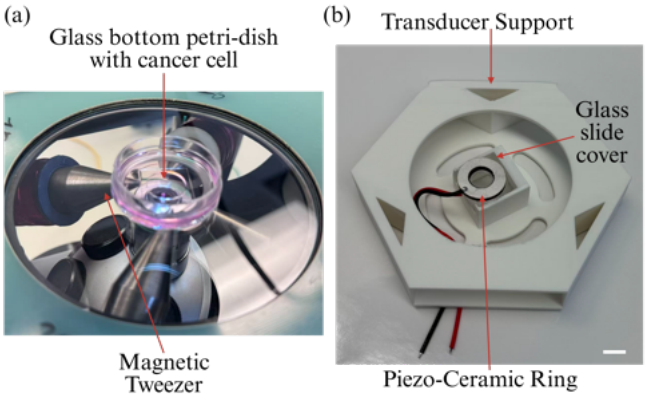

Fig. 3: The piezo-ceramic ring is attached to a 3d printed transducer support by a glass slide cover (b) to mount directly at the centre of the petri dish loaded with cell culture (a) scale bar = 10 mm

ultrasound at 1 MHz, driven by a function generator and an amplifier at 48 V_{pp}.

The piezo-ceramic transducer is affixed to a glass cover slide using acoustically transparent epoxy and mounted directly onto a standard 35-mm petri dish containing the cell culture. This top-down configuration ensures that the transducer surface is immersed in the culture medium, positioned precisely 2 mm above the bottom surface of the dish.

This setup enables localized acoustic excitation of MAMs within the magnetic workspace, allowing in situ mechanical stimulation of adherent cancer cells. The choice of 1 MHz operating frequency is motivated by its proven compatibility with microbubble resonance dynamics [14], [16], [17], which offers an optimal balance between spatial resolution and penetration depth in biological tissues. Previous studies have demonstrated that microbubbles can generate nanonewton-scale stimulation at these frequencies, sufficient to induce mechanotransduction or disrupt cellular membranes [18], [19], [20].

C. Microfluidic Device Fabrication

A flow-focusing microfluidic chip was designed and fabricated by standard soft lithography to generate 10 μm MAMs with controlled size and shell composition (Table 1). Briefly, a 4-inch Si wafer was coated with SU-8 2025 (5000 rpm, 30 s) to a target thickness of 15 µm, soft-baked at 95 °C, exposed on a maskless aligner (4× objective, 365 nm; focus offset 0.263 mm; 0.9 s), post-exposure baked at 95 °C, and developed to yield the channel master. PDMS (Sylgard 184; 10:1 base:curing agent) was mixed, degassed, cast on the master, and cured at 65 °C for 2 h. The PDMS layer was peeled, inlets/outlets were punched (0.5 mm), and the device was oxygen-plasma treated and irreversibly bonded to glass (Fig. 4b).

The final layout comprises a central gas inlet, two liquid side inlets, and a single outlet (Fig. 4a). During the experiment, nitrogen was supplied to the gas inlet (70

TABLE I: Microfluidic Device Parameters

Parameter	Value
Liquid inlet channel width	100 μm
Gas inlet channel width	50 μm
Channel depth	15 μm
Orifice (nozzle) width	10 μm
Gas pump pressure	70 kPa
Liquid flow rate	5 μL/min

kPa) and the liquid phases — 1,2-distearoyl-sn-glycero-3-phosphocholine (DSPC) and Fe_3O_4 iron-oxide nanoparticles (IONPs, 1 mg/mL in deionized water) — were delivered through the side channels by syringe pumps (5 μL/min). At the 10 μm flow-focusing orifice, the gas thread was pinched into discrete bubbles that acquired a stabilizing lipid–IONP shell (Fig. 4c)

MAM generation was visualized on an inverted microscope with a high-resolution CMOS camera; size distributions were quantified in MATLAB R2024b. Shell composition and IONP incorporation were assessed by Transmission Electron (TEM), following a previous protocol: MAM suspensions were deposited on carbon-coated copper grids and negatively stained to enhance lipid–IONP contrast. The generated MAMs were observed using an inverted microscope equipped with a high-resolution CMOS camera. MATLAB R2024b image processing tools were used to evaluate the MAM size distribution. TEM was employed to evaluate the shell composition and confirm ion oxide nanoparticle incorporation, following the methodology outlined by Owen and Stride in their protocol for phospholipid microbubble coating analysis [21]. Specifically, MAM suspension is deposited onto carbon-coated copper grids and negatively stained to enhance lipid-IONP contrast.

D. Cancer Cell Experiment

MDA-MB-231, a metastatic breast cancer cell line, was obtained from the American Type Culture Collection (ATCC, USA). Cells were cultured in T-75 flasks using MDA medium [F-12K (Gibco, USA) supplemented with 10 % fetal bovine serum (FBS) (Wisent, Canada) and 1 % penicillin-streptomycin (P/S) (Wisent, Canada)]. Cultures were kept at $37°C$ in a humidified incubator with 5 % CO2 and passaged every 3 days, up to passage 25. For the subculture, confluent cells were removed with 0.25 trypsin-EDTA (Wisent, Canada), collected by centrifugation (7 min at 1200 rpm), and counted using a hemocytometer. The experiments were carried out in 35mm glass-bottom culture plates seeded at a density of 3.0×10^5 cells/dish in 2 ml of medium. After stimulation, cells were incubated for an additional 24 hours for the viability analysis.

III. METHODS

A. Microfluidic Fabrication of MAMs

Delivering controllable and reproducible mechanical stimulation requires (i) precise size control so each magnetic–acoustic microbubble (MAM) resonates near the driving frequency, and (ii) stable loading of iron-oxide nanoparticles (IONPs) into the lipid shell without compromising interfacial stability. Bulk emulsification (e.g., agitation/sonication) yields highly polydisperse bubbles, producing non-uniform oscillation amplitudes and inconsistent mechanical output [22], [23]; meanwhile, uneven IONP incorporation can precipitate shell failure and loss of both magnetic and acoustic responsiveness [11], [24].

To overcome these limitations, we employed a flow-focusing microfluidic device (see Systems and Experiments session for the detailed fabrication process), which enables hydrodynamic control of bubble breakup (Fig. 9). In this microfluidic system (Fig. 4c), a central nitrogen gas stream is pinched by two lipid–IONP liquid streams at a narrow orifice ($w_o = 10\mu m$). The dynamics of bubble formation are governed by the capillary number,

$$\mathrm{Ca} = \frac{\mu U}{\gamma}, \tag{1}$$

where μ is the dynamic viscosity of the fluid, U the mean liquid velocity at the orifice, and γ is the gas–liquid surface tension. In the regime $\mathrm{Ca} < 1$, interfacial tension dominates, and the breakup process yields highly monodisperse bubbles. This regime is critical for achieving reproducible microbubble sizes.

The resulting microbubble diameter d_b can be empirically expressed as a function of the orifice width w_o and the gas-to-liquid flow-rate ratio $\phi = Q_g/Q_l$:

$$d_b \approx C w_o \phi^{\alpha}, \tag{2}$$

where C is a geometry-dependent constant and $\alpha \in [0.3, 0.5]$ for gas–liquid microfluidic systems. By operating in this predictable scaling regime, the device consistently generated MMBs within 8–12 μm. This fabricated size is close and centered around 10 μm, whose theoretical acoustic resonance range at around 1 MHz [14].

A second challenge arises from the incorporation of iron-oxide nanoparticles (IONPs) into the lipid shell. The orifice width is only 10 μm, meaning even micron-scale aggregates or microbial contaminants can easily accumulate and then block the channel. This not only interrupts MAM formation but also destabilizes the lipid shell. To prevent clogging, we implemented a passive filtration structure at the entrance of both liquid inlets, inspired by recent advances in geometric microfluidic separation [25]. The filter consists of periodic micro-post arrays that remove particles and debris larger than 20 μm before entering the main channel, thereby ensuring smooth flow and homogeneous nanoparticle loading.

These two strategies eliminate size polydispersity and aggregation-induced clogging, enabling stable production of monodisperse MAMs with diameters of approximately 10 μm and uniform lipid-IONP distribution. The MAMs maintained acoustic responsiveness and structural stability, making them suitable for subsequent magnetic manipulation and ultrasound-driven mechanical stimulation.

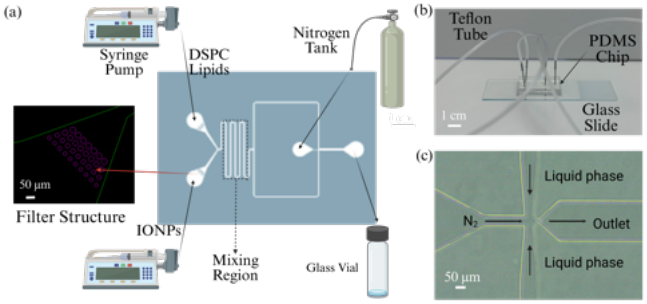

Fig. 4: Fabrication of MAMs in a flow-focusing microfluidic device. (a) Schematic of the flow-focusing device showing inputs of DSPC lipid solution, iron-oxide nanoparticle (IONP) solution, and nitrogen gas, the liquid inlet filter structure, and the collection of MAMs at the outlet. Syringe pumps control liquid flow rates, while a nitrogen tank with a pressure gauge supplies the gas phase. (b) Picture of an assembled PDMS–glass microfluidic chip; the inlets and the outlet are connected to Teflon tubes (0.6 mm inner diameter) via 0.6 mm blunt needles. (c) Optical microscope image of the flow-focusing orifice for MAM formation, imaged under a 10× objective lens.

B. Modeling of the Quadrupole Magnetic Tweezers and Microbubble Dynamics

Precise manipulation of MAM to apply mechanical stimulation to cancer cells requires generating sufficiently high and uniform magnetic field gradients in a confined workspace, accurately modeling the magnetic field distribution for real-time force estimation, and capturing the coupled dynamics between magnetic, hydrodynamic, and buoyancy forces at the microscale. To meet these requirements, we adopt a physical modeling approach grounded in magnetic monopole theory and validated through finite element simulations and experimental calibration.

1) Magnetic Field Modeling: Inspired by the analytical framework proposed by [15] and [26], we model the quadrupole magnetic tweezer configuration using the virtual magnetic charge model. Although magnetic monopoles do not exist in nature, modeling the coils as point "magnetic charges" q_i at predefined locations offers a tractable yet effective method for predicting the magnetic field $B_{(r)}$:

$$B(r) = \sum_{i=1}^{4} \frac{\mu_0 q_i}{4\pi r_i^2} \hat{r}_i, \tag{3}$$

where $r_i = |\mathbf{r} - \mathbf{r}_i|$ is the distance from the i-th source to the field point, and $\hat{\mathbf{r}}_i$ is the corresponding unit vector. This method allows effective computation of field distributions and serves as a foundation for magnetic force and trajectory planning.

2) Modeling of the Induced Magnetic Moment: When actuated, MAMs are magnetized and its magnetic moment interacts with the control magnetic field. We model the induced magnetic moment m_{MAM} using the linear isotropic susceptibility model:

$$m_{MAM} = V_{\text{MAM}} \frac{\chi_m}{\mu_0} B, \tag{4}$$

where V_{bubble} is the MAM volume and χ_m is its magnetic susceptibility. This formulation simplifies numerical treatment and directly integrates with force computation models.

3) Magnetic Force Computation: The magnetic force exerted on the MAM is derived from the gradient of the magnetic potential energy:

$$F_{mag} = \nabla(m_{MAM} \cdot B) = \frac{V_{\text{MAM}} \chi_m}{\mu_0} \nabla(B \cdot B), \tag{5}$$

This equation highlights the dependency of force on the spatial variation (gradient) of the magnetic field magnitude. Near the center of the workspace, the field $\mathbf{B}$ can be approximated as a linear function of the coil currents $I = [I_1, I_2, I_3, I_4]^\top$. Introducing a normalized current vector $\hat{I} = I/I_{\max}$ and a constant matrix N_0 encoding system geometry and material factors, we simplify the force model at the center as:

$$F_c = k_i \nabla \left(\hat{\mathbf{I}}^\top N_0 \hat{\mathbf{I}} \right), \tag{6}$$

This compact form enables real-time optimization of I to generate desired force vectors for MAM manipulation.

4) MAM Dynamics under Combined Forces: Modeling the MAM's motion requires integrating the magnetic force with other microscale forces, including viscous drag, gravity, and buoyancy (Fig. 5b). The full equation of motion is expressed as:

$$m\frac{d^2 r}{dt^2} = F_{mag} + 6\pi\eta r \frac{dr}{dt} + mg\hat{z} + \rho_{\text{fluid}} g V_{\text{MAM}} \hat{z}, \tag{7}$$

where m is the mass of the MAM, η is the fluid viscosity, and r is MAM's radius. The gravitational and buoyant forces act along the vertical axis, introducing vertical drift components that must be compensated for in trajectory control.

5) Validation of the Generated Magnetic Field and the Analytical Model: To validate the accuracy of the field model and assess actuation performance, we conducted a finite element simulation using COMSOL Multiphysics 6.1. A single corner coil was activated at **3 A** to generate a localized magnetic flux, visualized via heatmaps (Fig. 5a). The predicted field was verified against experimental calibration using a Hall-probe Gauss meter (Figure 5c), the uncertainty between the simulation results and actual measurements comes from the impurity of the iron rod that we use to fabricate the magnetic tweezer. The estimated field gradient ranged between 0.6 and 0.8 T/m across the workspace (Fig. 5d), which matches well with theoretical expectations. By leveraging the principle of superposition, the combined magnetic field generated by all four coils can produce a spatial field gradient as high as 2–3 T/m across the workspace. The equation of motion described in Eq. (7) can be solved by ODE15s solver in MATLAB R2024b, and the calibrated gradient field is sufficient to generate magnetic forces that overcome viscous drag and buoyant

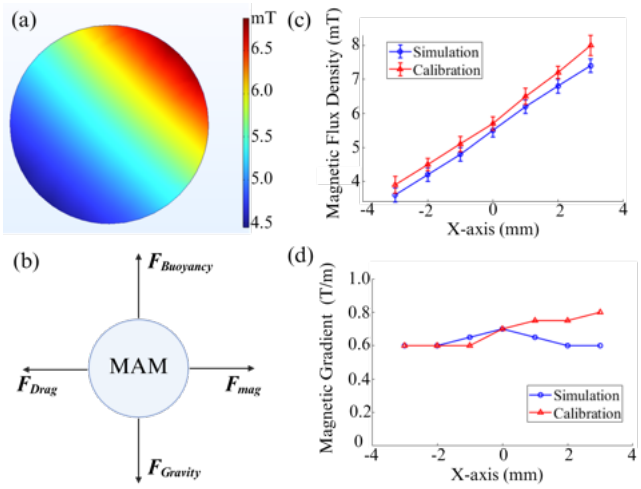

Fig. 5: (a) FEA simulation results within the 6 mm workspace when activating one pole of the magnetic tweezer, (b) Free body diagram of the MAM in liquid. The simulation and calibration results of magnetic flux density (c), and the computed magnetic field gradient (d).

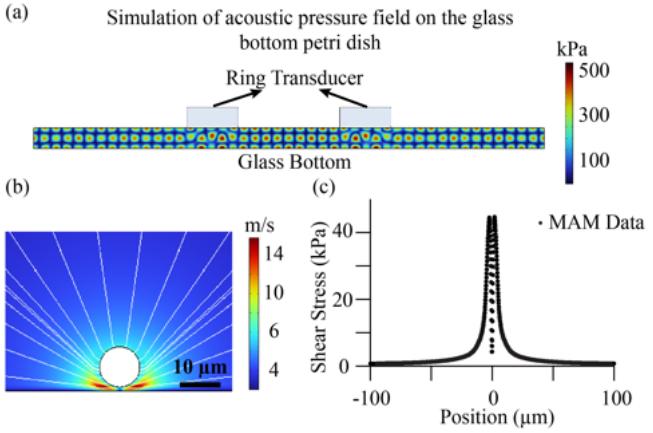

Fig. 6: (a) FEA simulation of the acoustic pressure field in liquid induced by the ring transducer. (b) FEA simulation of the local microstreaming pattern around a single MAM. (c) Shear stress induced by the streaming flow on the glass bottom $\pm 100\mu m$ from the center of MAM.

forces, enabling stable and controllable microbubble motion.

C. Acoustic Modeling for MAM Oscillation

Acoustic microbubbles have been used to excite adherent cells in liquid, but three factors limit control and interpretation. First, the microbubble dynamics under the acoustic field are highly non-linear, and a lack of an effective experimental calibration method limits the prediction of corresponding biophysical effects [27], [28]. Second, the localized microstreaming flows generated by microbubbles can induce shear stresses on nearby cells, which are difficult to characterize both experimentally and numerically due to the microscale geometry and transient nature of the field [29], [30]. Finally, accurately predicting the biophysical response of cells to this localized shear stress remains an open problem, especially when considering interactions with compliant or deformable substrates [31], [32].

Here, we adopt a multi-physics modeling approach that couples nonlinear microbubble oscillation dynamics with the incompressible Navier–Stokes equations to estimate local streaming patterns and shear stress distributions. This modeling framework builds upon recent advances in acoustic microbubble modeling [33], [34].

1) Nonlinear Bubble Oscillation Under Acoustic Excitation: Microbubble oscillation is governed by the internal gas pressure, external acoustic driving pressure, surface tension, viscous drag, and shell viscoelasticity. The instantaneous pressure on the MAM surface is defined as:

$$P_b = \left(P_0 + \frac{2\gamma}{R_0}\right)\left(\frac{R_0}{R}\right)^{3k} - \frac{2\gamma}{R} - \frac{4\mu\dot{R}}{R} - \frac{2k_s R}{R^2} - 4\xi\left(\frac{1}{R_0} - \frac{1}{R}\right) - P(t) \tag{8}$$

Here, R and R_0 are the instantaneous and initial radii of the MAM, μ is the dynamic viscosity of the fluid, γ is surface tension, k is the polytropic gas index ($k = 1.07$), k_s and ξ represent the shell stiffness and damping coefficient, respectively, and $P(t)$ is the time-varying external acoustic pressure. This equation provides a physical approach to compute the oscillation amplitude of the MAM and serves as the primary input for modeling acoustic streaming.

2) Acoustic Field and Streaming-Induced Shear Stress: In our experimental configuration, a piezoelectric ring transducer is driven at 1 MHz with a peak-to-peak voltage of 48V. This setup can generate an acoustic field with a maximum pressure amplitude of approximately 500 kPa in the liquid medium, as verified via simulation (Fig. 6a).

To model the resultant microstreaming, we couple the pressure on the surface of the microbubble (P_b) to the incompressible Navier-Stokes equation, assuming a low Reynolds number and negligible compressibility. The MAM-induced streaming creates rotational flow structures near the substrate, which are particularly significant for MAMs located adjacent to the bottom surface of the Petri dish (where adherent cancer cells reside). As shown in (Fig. 6b), these localized streaming flows generate non-uniform shear stress distributions. Quantitative simulation results reveal shear stresses exceeding 50 kPa in regions within 10 μm of the MAM surface (Fig. 6c). These stress levels are sufficient to translate mechanobiological stimulation to target cells, demonstrating the feasibility of this actuation method for cellular manipulation and stimulation.

IV. Results

A. MAM Production and Characterization

MAMs are fabricated using our custom-designed flow-focusing microfluidic device. The MAMs are pinched off through the orifice (Fig. 7a) and accumulated at the outlet and

were collected in a 5 ml glass vial for subsequent analysis (Fig. 7b).

In characterization, 10 μL of the floating layer of freshly generated MAMs is extracted by a pipette transfer and diluted in phosphate-buffered saline (PBS) (1:10 ratio) to reduce concentration and minimize overlapping during imaging. Bright-field microscopy at 10× magnification enabled visualization of both undiluted and diluted samples (Fig. 7c and 7d), highlighting the stability and spherical morphology of the MAMs. TEM images of MAMs in (Fig. 7f) demonstrates the deposition of DSPC lipid layers with embedded iron oxide nanoparticles, which corresponds to the successful incorporation of the lipid–IONP shell on MAM. Although the discontinuities on the coating could be seen, clusters of IONPs are still visible at higher magnification.

The size distribution of the diluted MAMs was quantified by processing 10 random microscopy images using the MATLAB R2024b image processing toolkit. Approximately 200 MAMs were detected and fitted to a normal distribution, yielding a mean diameter of 9.8 μm with a standard deviation of 1.8 μm (Fig. 7e). TEM images of the MAMs in (Fig. 7f) demonstrate the deposition of DSPC lipid layers with embedded iron oxide nanoparticles, which corresponds to the successful incorporation of the lipid–IONP shell on MAM. Although the discontinuities in the coating could be seen. These results confirmed that the flow-focusing microfluidic approach produced monodisperse MAMs suitable for acoustic and magnetic actuation studies.

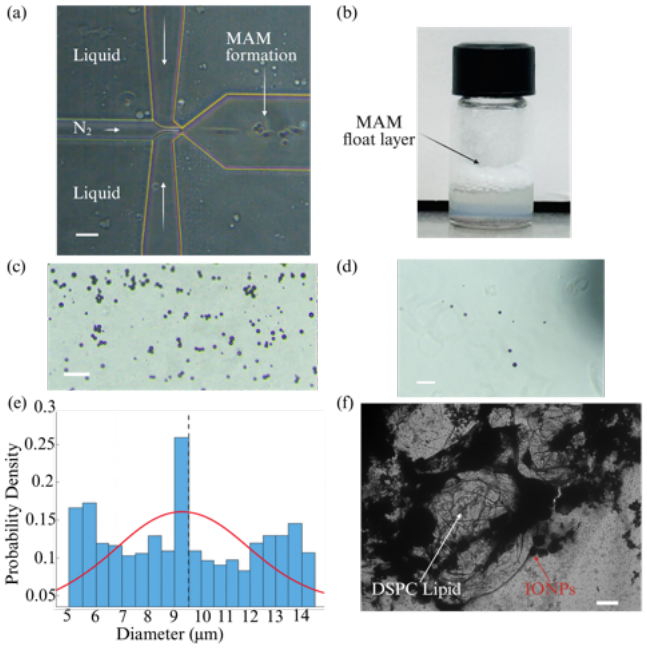

Fig. 7: (a) MAM formation at the microfluidic orifice, scale bar = 50 μm. (b) Collected MAMs accumulate at the floating layer in a glass vial. Bright-field microscopy image of undiluted (c) and diluted MAMs (d), scale bar = 50 μm. (e) Size distribution histogram with Gaussian fit (mean: 9.8 μm, std: 1.8 μm). (f) TEM image showing DSPC lipid layer and embedded IONPs in the shell, scale bar = 2 μm.

B. Magnetic Actuation of MAM

The quadrupole magnetic tweezer system was configured to generate a strong diagonal magnetic field gradient across the desired workspace. Specifically, the coil at the lower right corner was driven at +3 A, while the remaining three coils were set to -3 A, resulting in a net magnetic gradient directed along the diagonal axis (Fig. 8a). A single MAM with a diameter of approximately 13.8 μm was selected for magnetic actuation under the magnetic field.

Upon activation of the magnetic field, the MAM translated along the expected direction, achieving a total displacement of 160 μm within 50 s. The trajectory was recorded in real time at 30 frames per second, with position tracking performed in MATLAB. The target trajectory and experimentally recorded path are shown in Fig. 8b. Despite minor deviations from the ideal path, the maximum uncertainty between the real-time trajectory and the target trajectory was 9.9 μm, which is smaller than the body size of the manipulated MAM. These results indicate that the quadrupole magnetic tweezer system provides stable and accurate magnetic actuation at the single-MAM scale.

C. Cancer Cell stimulation by MAM

Cell experiments were performed in 35-mm glass-bottom dishes seeded at 3.0×10^5 cells per dish in 2 mL of medium. Six dishes were prepared per run and assigned to three conditions (n = 2 technical replicates per group): (i) static control (no treatment), (ii) ultrasound only, and (iii) MAM-coupled ultrasound. For the MAM-coupled group, 100 μL of diluted MAM suspension was added to each 2 mL dish, and MAMs were magnetically guided to the vicinity of the cell monolayer using the quadrupole magnetic tweezer system. All exposed dishes then received a 1 MHz ultrasound field for 1 min to induce MAM oscillation in proximity to cells; the static control received no insonation. Following treatment, dishes were returned to the incubator. Following treatment with MAM-enhanced acoustic stimulation, cancer cell viability was assessed at 0, 12, and 24 hours across three groups: Control group, acoustic-only group, and MAM + acoustic group. Quantitative analysis of viable cells from ten randomly selected microscopy images per condition per culture dish revealed a progressive and significant reduction in cell survival over time, with the treatment effect of lower cell viability observed in the MAM + acoustic group (Fig. 9).

At 0 hour (right after treatment), the MAM + Acoustic group exhibited a significant decrease in viability (Control vs. MAM+Acoustic: 127.9 $\pm$ 37.2 vs. 103.9 $\pm$ 15.1 , $P = 0.008$; Acoustic-only vs. MAM + Acoustic: 127.4 $\pm$ 20.7 vs. 103.9 $\pm$ 15.1, $P = 0.001$), while the acoustic field alone did not affect the cell viability (Control vs. Acoustic only: 127.9 $\pm$ 37.2 vs. 127.4 $\pm$ 20.7, $P = 0.96$).

At 12 hours post-treatment, the MAM + Acoustic group exhibited a significant decrease in viability (Control vs.

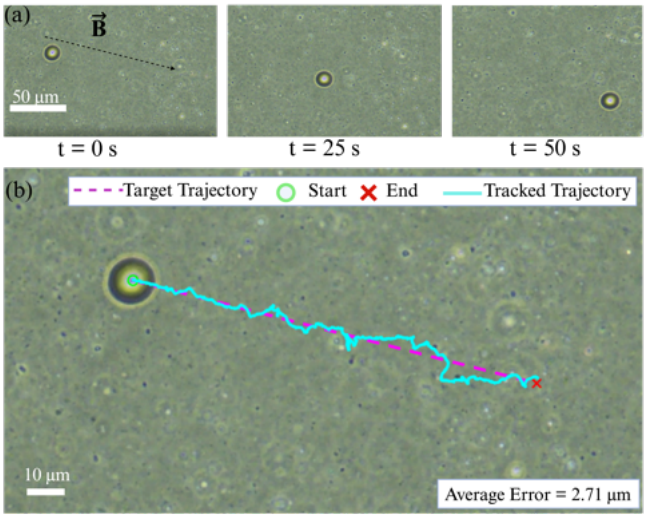

Fig. 8: (a) Time-lapsed images of an MAM under a 20× objective lens at t = 0, 25, and 50 s, showing translation along the applied diagonal magnetic field. (b) Comparison of the targeted versus tracked trajectory of the MAM, recorded at 30 fps.

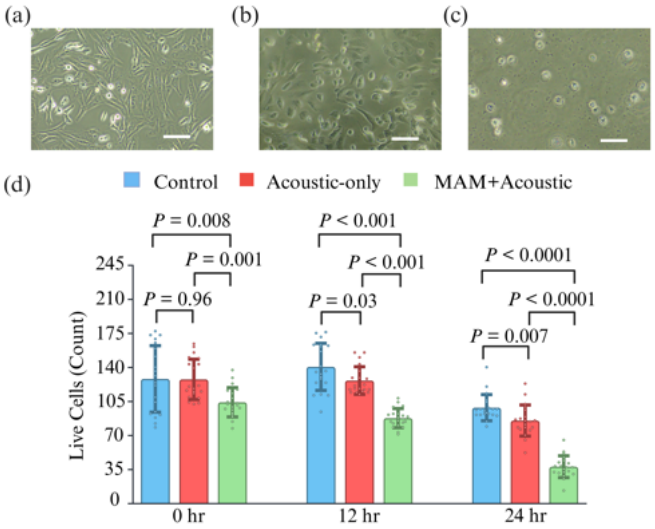

Fig. 9: Effect of MAM-based stimulation on cancer cell viability. a) Bright-field image of the control group showing healthy morphology. b) Acoustic-only group shows partial detachment. c) MAM + Acoustic stimulation group shows major disruption and collapse. d) Quantification of viable cells across conditions and time points. All figures are imaged after 24-hour post-stimulation. N = 20 captured images per column. Error bar: standard deviation. Scale bar = 100 μm.

MAM + Acoustic: 140.3 $\pm$ 24.2 vs. 87.6 $\pm$ 9.8, $P < 0.001$; Control vs. Acoustic-only: 140.3 $\pm$ 24.2 vs. 126.2 $\pm$ 14.2, $P = 0.03$; Acoustic-only vs. MAM + Acoustic: 126.2 $\pm$ 14.2 vs. 87.6 $\pm$ 9.8, $P < 0.001$). This translates to a 35.4% lower mean viability in the MAM group compared to the control and a 30.7% reduction compared to acoustic-only, indicating a more pronounced cytotoxic effect.

At 24 hours, the disparity widened further. The Static group maintained moderate viability (mean = 98.3 $\pm$ 13.5), while Acoustic-only showed mild decline (mean = 85.1 $\pm$ 16.0). In contrast, the MAM + Acoustic group showed a dramatic drop (mean = 37.6 $\pm$ 11.2; Control vs. MAM + Acoustic: $P < 0.0001$; Acoustic-only vs. MAM + Acoustic: $P < 0.0001$; Control vs. Acoustic-only: $P = 0.007$), amounting to a 61.7% reduction in mean viable cells relative to control, and a 55.8% reduction compared to Acoustic-only. These differences were consistent across replicate images and statistically significant.

V. Conclusions and Discussions

In this paper, we present a magneto–acoustic platform that employs microfluidically fabricated, shell-engineered magnetic–acoustic microbubbles (MAMs) to deliver targeted and repeatable mechanical stimulation to cancer cells. The core novelty lies in integrating (i) microfluidic flow-focusing to produce narrowly distributed, $\sim$ 10 μm bubbles with resonance set by size and with iron-oxide nanoparticle (IONP) loading, and (ii) magnetic and acoustic field models that guide a custom magneto–acoustic actuation system to precisely navigate MAMs and generate strong mechanical stimulation. Leveraging precise magnetic navigation and strong acoustic actuation, the mechanical stimulation generated by MAMs produced a reduction in cancer cell viability.

Nevertheless, limitations remain in coating magnetic nanoparticles onto the lipid shell, which is constrained by the concentration of the IONP solution introduced into the microfluidic device. The extremely small orifice (10 μm) restricts loading capacity and thus limits the magnetic susceptibility of the MAMs. To enable future closed-loop control of MAMs in three dimensions—including high-precision vertical positioning—higher effective nanoparticle concentrations or alternative surface-functionalization strategies will be required to further enhance magnetic responsiveness.

References

[1] A. Kumari, S. M. Veena, R. Luha, and A. Tijore, "Mechanobiological strategies to augment cancer treatment," *ACS Omega*, vol. 8, no. 45, pp. 42 072–42 085, 2023.

[2] A. Agrawal, Y. Javanmardi, S. A. Watson, B. Serwinski, B. Djordjevic, W. Li, A. R. Aref, R. W. Jenkins, and E. Moeendarbary, "Mechanical signatures in cancer metastasis," *npj Biological Physics and Mechanics*, vol. 2, p. 3, 2025.

[3] A. J. Clevenger, "Advances in cancer mechanobiology: Metastasis, mechanics, and materials," *APL Bioengineering*, vol. 8, no. 1, p. 011502, 2024.

[4] X. Wang, C. Ho, Y. Tsatskis, J. Law, Z. Zhang, M. Zhu, C. Dai, F. Wang, M. Tan, S. Hopyan, H. McNeill, and Y. Sun, "Intracellular manipulation and measurement with multipole magnetic tweezers," *Science Robotics*, vol. 4, no. 31, p. eaav6180, 2019.

[5] Y. Gao, C. Chan, Q. Gu, Y. Chen, L. Li, S. Liu, and H. Cheng, "Controlled nanoparticle release from stable magnetic microbubble oscillations," *NPG Asia Materials*, vol. 8, p. e260, 2016.

[6] Y. Deng, A. Paskert, Z. Zhang, R. Wittkowski, and D. Ahmed, "An acoustically controlled helical microrobot," *Science Advances*, vol. 9, no. 38, p. eadh5260, 2023.

[7] A. Ozcelik, J. Rufo, F. Guo, Y. Gu, P. Li, J. Lata, and T. J. Huang, "Acoustic tweezers for the life sciences," *Nature Methods*, vol. 15, pp. 1021–1028, 2018.

[8] X. Ju, C. Chen, C. M. Oral, S. Sevim, R. Golestanian, M. Sun, N. Bouzari, X. Lin, M. Urso, J. S. Nam, Y. Cho, X. Peng, F. C. Landers, S. Yang, A. Adibi, N. Taz, R. Wittkowski, D. Ahmed, W. Wang, V. Magdanz, M. Medina-Sánchez, M. Guix, N. Bari, B. Behkam, R. Kapral, Y. Huang, J. Tang, B. Wang, K. Morozov, A. Leshansky, S. A. Abbasi, H. Choi, S. Ghosh, B. B. Fernandes, G. Battaglia, P. Fischer, A. Ghosh, B. J. Sánchez, A. Escarpa, Q. Martinet, J. Palacci, E. Lauga, J. Moran, M. A. Ramos-Docampo, B. Städler, R. S. H. Restrepo, G. Yossifon, J. D. Nicholas, J. Ignés-Mullol, J. Puigmartí-Luis, Y. Liu, L. D. Zarzar, C. W. S. IV, L. Li, S. Li, X. Ma, D. H. Gracias, O. Velev, S. Sanchez, M. J. Esplandiu, J. Simmchen, A. Lobosco, S. Misra, Z. Wu, J. Li, A. Kuhn, A. Nourhani, T. Maric, Z. Xiong, A. Aghakhani, Y. Mei, Y. Tu, F. Peng, E. Diller, M. S. Sakar, A. Sen, J. Law, Y. Sun, A. Pena-Francesch, K. Villa, H. Li, D. E. Fan, K. Liang, T. J. Huang, X.-Z. Chen, S. Tang, X. Zhang, J. Cui, H. Wang, W. Gao, V. K. Bandari, O. G. Schmidt, X. Wu, J. Guan, M. Sitti, B. J. Nelson, and S. Pané, "Technology roadmap of micro/nanorobots," *ACS Nano*, vol. 19, no. 27, 2025.

[9] Y. Guo, H. Lee, C. Kim, C. Park, A. Yamamichi, P. Chuntova, M. Gallus, M. O. Bernabeu, H. Okada, H. Jo, and C. Arvanitis, "Ultrasound frequency-controlled microbubble dynamics in brain vessels regulate the enrichment of inflammatory pathways in the blood-brain barrier," *Nature Communications*, vol. 15, p. 8021, 2024.

[10] E. Beguin, J. Sheng, H. Nesbitt, J. Owen, A. McHale, J. Callan, and E. P. Stride, "Magnetic targeting of oxygen loaded microbubbles for sonodynamic therapy," *The Journal of the Acoustical Society of America*, vol. 140, no. 4, pp. 3026–3036, 2016.

[11] E. Beguin, L. Bau, S. Shrivastava, and E. Stride, "Comparing strategies for magnetic functionalization of microbubbles," *ACS Applied Materials & Interfaces*, vol. 11, no. 2, pp. 1829–1840, 2019.

[12] M. Lee, E. Y. Lee, D. Lee, and B. J. Park, "Stabilization and fabrication of microbubbles: applications for medical purposes and functional materials," *Soft Matter*, vol. 11, no. 18, pp. 3069–3083, 2015.

[13] J. M. McNeill, N. Nama, J. M. Braxton, and T. E. Mallouk, "Wafer-scale fabrication of micro- to nanoscale bubble swimmers and their fast autonomous propulsion by ultrasound," *ACS Nano*, vol. 14, no. 6, pp. 6331–6341, 2020.

[14] Y. Sun, D. E. Kruse, P. A. Dayton, and K. W. Ferrara, "High-frequency dynamics of ultrasound contrast agents," *IEEE Transactions on Ultrasonics, Ferroelectrics, and Frequency Control*, vol. 52, no. 11, pp. 1981–1991, 2005.

[15] X. Wang, M. Luo, H. Wu, Z. Zhang, J. Liu, and Z. Xu, "Three-dimensional robotic control of a 5-micrometer magnetic bead for intra-embryonic navigation and measurement," *IEEE Transactions on Robotics*, vol. 33, no. 1, pp. 240–247, 2017.

[16] B. Helffield, J. J. Black, B. Qin, J. Pacella, X. Chen, and F. S. Villanueva, "Fluid viscosity affects the fragmentation and inertial cavitation threshold of lipid encapsulated microbubbles," *Ultrasound in Medicine & Biology*, vol. 42, no. 3, pp. 782–794, 2016.

[17] J. Kim, B. D. Lindsey, W.-Y. Chang, X. Dai, J. M. Stavas, P. A. Dayton, and X. Jiang, "Intravascular forward-looking ultrasound transducers for microbubble-mediated sonothrombolysis," *Scientific Reports*, vol. 7, p. 3454, 2017.

[18] Z. Fan, Y. Sun, D. Chen, D. Tay, W. Chen, C. X. Deng, and J. Fu, "Acoustic tweezing cytometry for live-cell subcellular modulation of intracellular cytoskeleton contractility," *Scientific Reports*, vol. 3, p. 2176, 2013.

[19] M. Zhang, S. Zhang, J. Shi, Y. Hu, S. Wu, Z. Zan, P. Zhao, C. Gao, Y. Du, Y. Wang, F. Lin, X. Fu, D. Li, P. Qin, and Z. Fan, "Cell mechanical responses to subcellular perturbations generated by ultrasound and targeted microbubbles," *Acta Biomaterialia*, vol. 155, pp. 211–224, 2022.

[20] Y. Gao, J. Lim, S.-H. Teoh, and C. Xu, "Emerging translational research on magnetic nanoparticles for regenerative medicine," *Chemical Society Reviews*, vol. 44, no. 17, pp. 6306–6329, 2015.

[21] J. Owen and E. Stride, "Technique for the characterization of phospholipid microbubbles coatings by transmission electron microscopy," *Ultrasound in Medicine & Biology*, vol. 41, no. 12, pp. 3253–3258, 2015.

[22] H. Li, Y. Yang, M. Zhang, L. Yin, J. Tu, X. Guo, and D. Zhang, "Acoustic characterization and enhanced ultrasound imaging of long-circulating lipid-coated microbubbles," *Journal of Ultrasound in Medicine*, vol. 37, no. 4, pp. 1017–1028, 2018.

[23] S. Sirsi, J. Feshitan, J. Kwan, S. Homma, and M. Borden, "Effect of microbubble size on fundamental mode high frequency ultrasound imaging in mice," *Ultrasound in Medicine & Biology*, vol. 36, no. 6, pp. 935–948, 2010.

[24] Z. Liu, T. Lammers, J. Ehling, S. Fokong, J. Bornemann, F. Kiessling, and J. Gätjens, "Iron oxide nanoparticle-containing microbubble composites as contrast agents for mr and ultrasound dual-modality imaging," *Biomaterials*, vol. 32, no. 26, pp. 6155–6163, 2011.

[25] H. Tang, J. Niu, H. Jin, S. Lin, and D. Cui, "Geometric structure design of passive label-free microfluidic systems for biological micro-object separation," *Microsystems & Nanoengineering*, vol. 8, p. 62, 2022.

[26] Z. Zhang, K. Huang, and C. H. Menq, "Design, implementation, and force modeling of quadrupole magnetic tweezers," *IEEE/ASME Transactions on Mechatronics*, vol. 15, no. 5, pp. 704–713, 2010.

[27] K. Sarkar, "Dynamics of bubbles and ultrasound: Diagnostic imaging to blood pressure monitoring and tissue engineering," *Physical Review Fluids*, vol. 10, no. 3, p. 030501, 2025.

[28] J. Mondal, R. Lakkaraju, P. Ghosh, and M. Ashokkumar, "Acoustic cavitation-induced shear: a mini-review," *Biophysical Reviews*, vol. 13, pp. 1293–1308, 2021.

[29] A. Bakhtiari, B. Schumm, M. Schönfelder, and C. J. Kähler, "Investigating cell viability under shear stress in complex microstreaming flows generated by ultrasound-driven actuated microbubbles," *Flow*, vol. 5, 2025.

[30] O. Pattinson, S. B. Keller, and N. D. Evans, "An acoustic device for ultra high-speed quantification of cell strain during cell–microbubble interaction," *ACS Biomaterials Science & Engineering*, vol. 9, no. 2, pp. 1283–1292, 2023.

[31] Y. He, J. Xia, J. D. H. Mai, N. Upreti, L. P. Lee, and T. J. Huang, "Acoustic technologies for the orchestration of cellular functions for therapeutic applications," *Science Advances*, vol. 11, no. 19, p. eadu4759, 2025.

[32] V. Pereno, J. Lei, D. Carugo, and E. Stride, "Microstreaming inside model cells induced by ultrasound and microbubbles," *Langmuir*, vol. 36, no. 14, pp. 3770–3780, 2020.

[33] I. Beekers, T. van Rooij, M. D. Verweij, and M. Versluis, "Acoustic characterization of a vessel-on-a-chip microfluidic system for ultrasound-mediated drug delivery," *IEEE Transactions on Ultrasonics, Ferroelectrics, and Frequency Control*, vol. 65, no. 2, pp. 317–327, 2018.

[34] J. Mondal, R. Lakkaraju, P. Ghosh, and M. Ashokkumar, "Acoustic cavitation-induced shear: a mini-review," *Biophysical Reviews*, vol. 13, pp. 1293–1308, 2021.